Nano Research 2017, 10(2): 437–455
DOI 10.1007/s12274-016-1304-6
Research Article
ISSN 1998-0124
CN 11-5974/O4

Flexible highly-effective energy harvester via crystallographic and computational control of nanointerfacial morphotropic piezoelectric thin film

Chang Kyu Jeong[1,2,†,§], Sung Beom Cho[3,§], Jae Hyun Han[1], Dae Yong Park[1], Suyoung Yang[4], Kwi-Il Park[5], Jungho Ryu[6], Hoon Sohn[4] (✉), Yong-Chae Chung[3] (✉), and Keon Jae Lee[1] (✉)

[1] *Department of Materials Science and Engineering, Korea Advanced Institute of Science and Technology (KAIST), 291 Daehak-ro, Yuseong-gu, Daejeon 34141, Republic of Korea*
[2] *KAIST Institute for the NanoCentury (KINC), 291 Daehak-ro, Yuseong-gu, Daejeon 34141, Republic of Korea*
[3] *Division of Materials Science and Engineering, Hanyang University, 222 Wangsimni-ro, Seongdong-gu, Seoul 04763, Republic of Korea*
[4] *Department of Civil and Environmental Engineering, KAIST, 291 Daehak-ro, Yuseong-gu, Daejeon 34141, Republic of Korea*
[5] *Department of Energy Engineering, Gyeongnam National University of Science and Technology, 33 Dongjin-ro, Jinju, Gyeongnam 52725, Republic of Korea*
[6] *Functional Ceramic Group, Korea Institute of Materials Science (KIMS), 797 Changwon-daero, Seongsan-gu, Changwon, Gyeongnam 51508, Republic of Korea*
† *Present address: Department of Materials Science and Engineering, Materials Research Institute, The Pennsylvania State University, University Park, PA 16802, USA*
§ *These authors contributed equally to this work.*

Received: 1 August 2016
Revised: 20 September 2016
Accepted: 26 September 2016

KEYWORDS
energy harvesting, morphotropic phase boundary (MPB), piezoelectric, first-principles calculation, lead zirconium titanate (PZT)

ABSTRACT

Controlling the properties of piezoelectric thin films is a key aspect for designing highly efficient flexible electromechanical devices. In this study, the crystallographic phenomena of $PbZr_{1-x}Ti_xO_3$ (PZT) thin films caused by distinguished interfacial effects are deeply investigated by overlooking views, including not only an experimental demonstration but also *ab initio* modeling. The polymorphic phase balance and crystallinity, as well as the crystal orientation of PZT thin films at the morphotropic phase boundary (MPB), can be stably modulated using interfacial crystal structures. Here, interactions with MgO stabilize the PZT crystallographic system well and induce the texturing influences, while the PZT film remains quasi-stable on a conventional Al_2O_3 wafer. On the basis of this fundamental understanding, a high-output flexible energy harvester is developed using the controlled-PZT system, which shows significantly higher performance than the unmodified PZT generator. The voltage, current, and power densities are improved by 556%, 503%, and 822%, respectively, in comparison with the previous flexional single-crystalline piezoelectric device. Finally, the improved flexible generator is applied to harvest tiny vibrational energy from a real traffic system, and it is used to operate a commercial electronic unit. These results clearly indicate that atomic-scale designs can produce significant impacts on macroscopic applications.

Address correspondence to Hoon Sohn, hoonsohn@kaist.ac.kr; Yong-Chae Chung, yongchae@hanyang.ac.kr; Keon Jae Lee, keonlee@kaist.ac.kr

1 Introduction

Piezoelectric energy harvesting technology, which uses abundant mechanical energy to generate electricity, has been of prime interest in the field of self-powered electronics to avoid frequent battery recharging [1–4]. In particular, flexible piezoelectric generators are regarded as powerful candidates to harness tiny movements (e.g., traffic vibrations) and conform to curvilinear/corrugated surfaces (e.g., biological organs) [5, 6]. For these reasons, many researchers have put in significant efforts to develop flexible piezoelectric energy harvesters using ZnO nanostructures, polyvinylidene fluoride (PVDF) membranes, or $PbZr_{1-x}Ti_xO_3$ (PZT) films [1, 6–8]; however, thus far, their performances have been insufficient to drive practical applications such as Internet of Things (IoT) sensors and wireless communications.

Recently, to overcome weak piezoelectricity, diverse types of single-crystalline piezoceramic films with complicated stoichiometry have been applied to flexible harvesters for scavenging high-output energy [9–11]. However, such single crystalline films have critical problems with severe piezoelectric degradation related to domain size versus thickness, along with the detrimental effect of grinding [11–14]. Moreover, it is difficult to fabricate single crystals with thicknesses below ~10 μm, which limits both mechanical flexibility and vibrational responsivity [9]. Owing to their limitations and high cost [15], flexible single-crystalline systems are highly restricted to a narrow range of applications; therefore, the systems inevitably require new approaches to be established using microstructural-controlled polycrystalline piezoelectric systems.

Piezoelectric properties of polycrystalline materials are strongly dependent on crystal orientation, phase, and crystallinity [16–18]. These crystallographic variables play very crucial roles in boosting piezoelectricity efficiently because well-controlled polycrystalline films can exhibit excellent piezoresponses compared with single crystalline structures [15]. Although several basic studies have been reported in which the crystal orientation of widely used PZT films has been modified [18, 19], there is a considerable lack of systematic material studies regarding piezoelectric phase configuration and crystallinity. In particular, the morphotropic phase boundary (MPB, i.e., multiphase composition) in PZT thin films is almost unexplored owing to their unclear phasic behaviors and interfacial influences. In addition, most previous texturing controls have utilized complex thermo/atmo-kinetics [20, 21], intricate stress stimuli [22], or seed/buffer layers [23–25], which are irreproducible and unsuitable for device fabrication. These limitations in the crystallographic prediction for PZT films need to be resolved to achieve high-performance flexible piezoelectric energy harvesters based on systemically well-designed polycrystalline PZT films.

To modify the crystalline specifications of PZT and enhance the efficiency of a flexible energy harvester, we theoretically and experimentally investigated the crystallographic control of piezoelectric PZT thin films using substrate modulation. By introducing the first-principles calculation as well as energy formalism to investigate PZT interfacial nature, MPB-phasic deviation, the variance of orientation, and crystallinity in the PZT thin films were quantitatively examined, with lattice-scale energy states of nucleation effects and orbital hybridizations. This sophisticated *ab initio* modeling can be used to guide the methodology for improving piezoelectric energy devices, enabled by the computational interpretation of PZT crystallographic phenomena. On the basis of this quantum-mechanic simulation, we demonstrated that the performance of a crystallographic-controlled flexible PZT generator is eight times higher than that of a single-crystalline film generator. A flexible energy harvester was successfully fabricated and applied to the energy conversion of tiny vibrational modes, programmed by the real traffic system of an expressway bridge.

2 Experimental

2.1 Fabrication processes of PZT thin films and flexible energy harvesters

PZT is regarded as the best piezoelectric material because of its excellent dielectric and ferroelectric properties and its facile and cheap fabrication method. We used a sol–gel process to form PZT thin films owing to the innumerable advantages, including excellent composition control and uniform homogeneity for MPB,

as well as simple fabrication and low temperature for cost effectiveness [26]. Furthermore, it can also be easily applied to crystallographic texturing because the polymeric metal alkoxide species in the sol–gel solution serve well as molecular building blocks for crystallization, compared with vacuum deposition methods [18, 27]. In this study, PZT thin films were deposited on two different substrates by normal methoxyethanol-based sol–gel solution processes.

The PZT thin films were prepared using a conventional sol–gel solution process on double-side polished MgO wafers (500-μm-thick, (100) surface plane, American Elements Co.) and sapphire (Al_2O_3) wafer (430-μm-thick, *c*-plane (0001) surface orientation, Hi-Solar Co.). The concentration of the PZT sol–gel solution (MEMS Solution Co.) is about 0.4 M, and the Zr/Ti molar ratio is 52/48, which is the MPB composition. After solution spin casting on the wafers, pyrolysis was implemented in air environment at 450 ℃ to eliminate polymeric constituents from the as-deposited film. The deposition and pyrolysis processes were repeated several times to achieve a 2-μm-thick PZT thin film, followed by crystallization in O_2-rich atmosphere at 650 ℃. The PZT thin films on both wafers were firmly attached to polyethylene terephthalate (PET) substrates (125-μm-thick, Sigma-Aldrich) using an ultraviolet (UV) light-curable polyurethane acrylate (PUA)-based resin (Norland optical adhesive, Norland Products Inc.). After UV light exposure to the samples through the clear PET side, a two-dimensional (2D)-pulsed XeCl excimer laser (λ = 308 nm, square-shaped area of 625 μm × 625 μm) was utilized to irradiate the backside of the wafers for separating the flexible PET-attached PZT thin film from the rigid wafers. For the laser lift-off (LLO) process, the 308 nm-wavelength laser (duration time ~30 ns) penetrates each wafer from the backside because the laser photonic energy (4.02 eV) is significantly lower than the substrate band gap energy levels (7–10 eV). Consequently, the PZT thin film completely absorbs the laser energy at the substrate interface, followed by partial melting and dissociation of PZT owing to the lower band gap energy of PZT (3.2–3.6 eV) than the photonic energy of XeCl laser. The optimum optical power levels of the laser beam were ~31 and ~20 mW in the cases of PZT/MgO wafer and PZT/sapphire wafer, respectively. The power and energy density of the laser beam was detected using a photodetector (Coherent Co.). We use the (100) MgO wafer not only because of the crystalline coherency with PZT but also the common utilization in optics. Moreover, (0001) Al_2O_3 (*c*-plane) is widely used in the commercial LLO fabrication. We also obtained the X-ray diffraction (XRD) peaks of PZT thin films on the rest of the Al_2O_3 wafers with other surface planes (*m*-plane and *a*-plane), which also showed random orientation of PZT films (Fig. S1 in the Electronic Supplementary Material (ESM)). Furthermore, no other planes of Al_2O_3 with the exception of *c*-plane are reliable as first-principles calculation with DFT computation because only the *c*-plane has the database in the Vienna *ab initio* quantum mechanics package, as described in Section 2.2.

Interdigitated electrodes (IDEs) with a finger length of 1.3 cm, electrode width of 100 μm, inter-electrode gap of 100 μm, and 33 digitate pairs were fabricated on the flexible PZT thin film by Ti and Au sputtering (110-nm-thick) and standard photolithography. To protect the surface of PZT and electrodes from mechanical damage and electrical shock, the energy harvesters were coated with SU-8 photoresist (5-μm-thick, MicroChem) with metal contact holes patterning for wiring. Poling processes to make remnant polarization of the PZT thin films were performed using electric fields of about 90 $kV \cdot cm^{-1}$ overnight.

2.2 First-principles computational calculation of PZT thin-film systems

First-principles calculations were carried out by solving the Kohn–Sham equation with a plane-wave basis set, as implemented in Vienna *ab initio* simulation package (VASP) code [28]. The basis set of plane waves was expanded to a cut off energy of 400 eV. The projector-augmented wave (PAW) method was used to describe the interactions between the valence electrons and the atomic core [29]. For PAW calculations, the $5d^{10}6s^26p^2$, $3d^24s^1$, and $4d^25s^1$ electrons were treated as valence electrons for Pb, Ti, and Zr atoms, respectively. For Mg and Al, 2s2p orbitals were considered as core electrons, whereas only the 1s orbital was treated as a core electron in oxygen. The exchange correlation function was described with the Perdew–Burcke–

Ernzerhof form of the generalized gradient approximation [30].

We constructed the supercell model to investigate the substrate effect of MgO and Al_2O_3 on PZT. The MgO substrate was described as six layers of (001) slabs where the bottom three layers of the substrates were fixed to the lattice parameters of the bulk. On the constructed substrate, eight layers of PZT were deposited with rhombohedral and tetragonal phases. Similarly, the PZT on Al_2O_3 supercell consists of six layers of (0001) slabs of Al_2O_3 and eight layers of PZT. The bottom three layers of Al_2O_3 were kept fixed to the parameter of bulk Al_2O_3. A vacuum layer of at least 15 Å was introduced to eliminate the interaction between supercells. A Brillouin-zone integration for the supercells was made with the grids of Monkhorst–Pack 3 × 3 × 1 and 3 × 4 × 1 for PZT//MgO and PZT//Al_2O_3, respectively [31]. Owing to the inevitable differences of lattice symmetry between MgO (cubic) and Al_2O_3 (hexagonal scalenohedron), the Monkhorst–Pack grid sampling of PZT//Al_2O_3 should be slightly high to satisfy the accurate density of states (DOS) as well as the total energy order. All constituent atoms were fully relaxed until the maximum total Hellmann–Feynman forces were in the range of 0.01 eV·Å^{-1}.

For the interpretation of the stability of the interface, the interface energy E_γ was evaluated by

$$E_\gamma = \frac{1}{A}\left\{E_{tot} - N_{PZT}E_{PZT}^{bulk} - N_{sub}E_{sub}^{bulk}\right\} - \sigma_{PZT} - \sigma_{sub} \quad (1)$$

where E_{tot} is the total energy of the entire system, E_{PZT}^{bulk} and E_{sub}^{bulk} are the energies of the bulk state of PZT and substrates, respectively, and A is the area of each cell [32, 33]. The σ_{PZT} and σ_{sub} are the free surface energies of PZT and substrates, respectively. After subtracting the entire bulk energy and free surface energy terms from the total system energy, only the interfacial energy E_γ remains. The surface energy of each cell was calculated from a symmetric slab model, and all energy terms were calculated by the defined first-principles calculation.

2.3 Measurement of output signals

A variety of XRD data (θ–2θ, 2θ, ω, and finely narrow scans) were performed by Ultima IV (Rigaku), SmartLab (Rigaku), D/MAX-2500 (Rigaku), and X'Pert-PRO MRD (PANalytical). The field-dependent piezoelectric coefficients are measured using a thin film analyzer (TF 1000, aixACCT Systems) with laser interferometry, a voltage amplifier, and an optical table. Optional oscilloscopes could also be applied to the measurement. In order to evaluate d_{33} values, we used sandwich-type samples composed of indium tin oxide (ITO, bottom electrode)/PZT/Pt (top electrode) with an active area of 0.5 cm^2. The bottom electrode on PET should be selected as a UV-transparent conductor because the PZT film should be attached on the PET by the UV-curable resin before LLO transfer (see Section 2.1, note that the Norland resin must be cured by UV penetrating through the PET). In addition, it should be noted that the laser interferometry-based film method is hardly applied directly to IDE-type devices. The flexible PZT thin-film energy harvesters were iteratively bent by a linear motor to measure the produced electrical signals. The applied strain to PZT thin film was calculated to be 0.3% by the mechanical equations. The voltage and current output were measured using a measuring device (2612A SourceMeter System, Keithley) and a low-noise current preamplifier (Model SR570, Stanford Research Systems). All measurement processes were conducted in a Faraday cage on an optical table (vibration isolation system) to leave out extraneous stimuli. To simulate electric signals of the energy harvesters in traffic systems, we used a function generator/mechanical vibrator system (Pasco Scientific Co.) and a waveform generator (33220A, Agilent Co.) that can read external programming motions. The input data of traffic vibrations were programmed by motion sensors at the 180-m-long Yeondae Bridge (distance between piers: ~45 m, width between crash walls: ~12.6 m) of Jungbunaeryuk (Central Inland) Expressway through Yeoju City (Republic of Korea). The average speed of vehicles was approximately 100 km·h^{-1}.

3 Results and discussion

3.1 Design and concept for crystallographic control of PZT thin film

Figure 1(a) shows the crystallographic-controlled piezoelectricity depending on MgO and sapphire

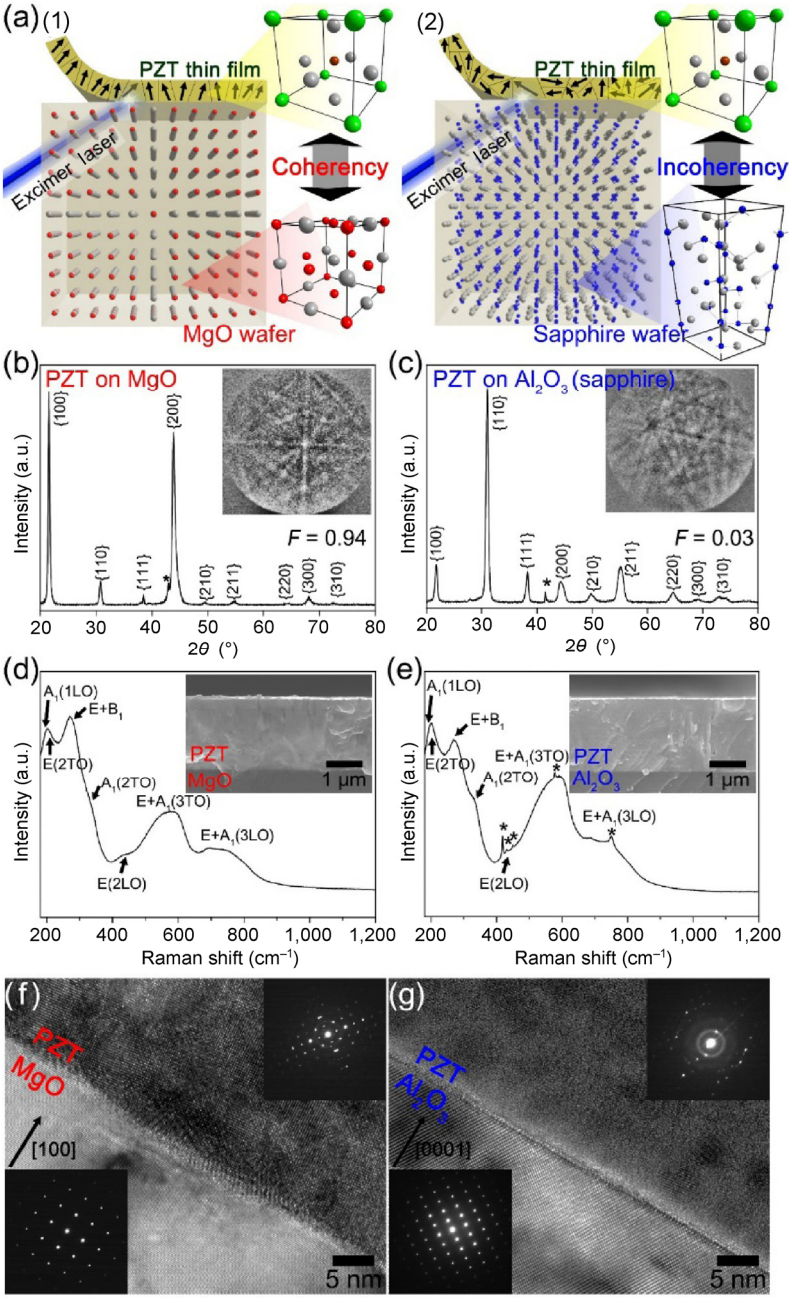

Figure 1 Conception and characterizations of crystallographic control of the PZT thin films in MPB. (a) Illustrations of the concept for crystallographic control over PZT thin films by simple wafer selection: (1) MgO and (2) sapphire wafer. The PZT thin films can be easily transferred onto flexible substrates by wafer-penetrating laser, i.e., laser lift-off. The arrows in the PZT thin films denote piezoelectric dipoles. For the sake of simplicity and unity, the commercial word "sapphire" is replaced by "Al_2O_3". (b) and (c) XRD patterns with θ–2θ scan mode of PZT thin films on (100) MgO and (0001) Al_2O_3 wafers. The asterisks denote the peaks from the bottom substrates, MgO and Al_2O_3. Insets: Kikuchi lines captured by EBSD of each PZT films. (d) and (e) Raman spectra of PZT films on the MgO and Al_2O_3 wafers. The asterisks denote the specific peaks from the Al_2O_3 wafer. Insets: cross-sectional SEM images of each PZT thin films. The inset indicates that the 2 μm-thick PZT thin films are equally deposited on both substrates by the same sol–gel method. (f) and (g) HRTEM images of PZT films on the MgO and Al_2O_3 wafers showing exact lattice configurations at their interfaces. The top and bottom insets display SAED patterns of wafer substrates and each PZT film, respectively. The slight tilt and expansion of PZT lattice on MgO is presumably caused by rhombohedral contents and interfacial lattice matching, respectively. The SAED patterns of PZT film on the Al_2O_3 wafer are vague and irregular, similar to a semi-amorphous crystalline film (the top inset of (g)), compared to the definite and uniform patterns of PZT on the MgO (the top inset of (f)).

(Al_2O_3) substrates for flexible PZT thin films transferred by laser. The PZT composition is selected as the MPB region of phase diagram (x ~ 0.48) because PZT with the MPB composition exhibits giant piezoelectric properties resulting from the maximized polarization rotation by the rhombohedral phase ($R3c$) coexisting with the tetragonal phase ($P4mm$) [34, 35]. As the crystal structure and lattice parameter of MgO (rock salt structure, a = 4.21 Å) are very similar to that of PZT (perovskite structure, 4.1–4.2 Å), the polycrystalline PZT thin film can be preferably oriented along the <100> crystallographic direction on the (100) MgO wafer, as illustrated in Fig. 1(a)(1). The preferred orientation of the PZT film on MgO can easily result in well-aligned piezoelectric domains, which improves polarization, as it does with single crystals [15, 17, 18, 36]. In particular, the <100> orientation of PZT has the highest piezoelectric response among all crystallographic directions throughout the entire PZT composition range including MPB [16]. Although the MgO wafer has been known as a simple substrate for textured PZT films, some difficult-to-control intermediate layers such as textured Pt have inevitably been used in previous reports due to the limitations of bare wafers in actual piezoelectric applications and device fabrications [25, 36–38]. In contrast, the Al_2O_3 wafer has an entirely different crystal structure (corundum structure, a = 4.78 Å and c = 12.99 Å), compared to that of PZT. Consequently, polycrystalline PZT film acquires a random orientation on the Al_2O_3 substrate, with weaker piezoelectricity than that of the textured PZT on MgO (Fig. 1(a)(2)). Importantly, the degree of lattice coherency between the PZT film and the respective substrate can be expected to affect additional crystallographic variables of the PZT, such as phase and crystallinity because film crystallization fluctuates and varies because of the interfacial characteristics in energy formalism. In this research, we theoretically investigate the diverse crystallographic issues of PZT films, which have been rarely studied owing to several intricate problems such as atomic-interfacial effects.

3.2 Analyses of crystal orientation, phase, and crystallinity of PZT thin film in MPB

Figure 1(b) shows the XRD data for the PZT thin film on the MgO wafer, obtained with the out-of-plane (θ–2θ) scan mode to detect the overall preferred orientation. The (100), (200), and (300) peaks are higher than the other orientation peaks, indicating that the polycrystalline PZT film on the (100) MgO wafer is well aligned in the <100> direction. As presented in Fig. 1(c), in contrast, the θ–2θ XRD pattern of the PZT film on the Al_2O_3 wafer confirms its random orientation, exhibiting powder-like XRD patterns. On the basis of Lotgering's theory [39, 40], the crystal orientation factor (F) can be calculated using the following equations

$$F = \frac{P - P_0}{1 - P_0} \tag{2}$$

$$P = \frac{\sum I_{(abc)}}{\sum I_{(hkl)}} \tag{3}$$

where P is the ratio of "intensity sum of concerned planes (abc)" to "intensity sum of total planes", and P_0 stands for the equivalent ratio for the ideal random orientation of powder XRD. The orientation factor of the PZT on MgO was evaluated to be about 0.94, showing its excellent preferred orientation, whereas the orientation factor of the PZT on Al_2O_3 was nearly zero (~0.03). We also performed ω-scan mode XRD (rocking curve) to observe the crystal orientation quality of each PZT thin film [41]. Figure S2 in the ESM shows the ω-scan data of PZT//MgO and PZT//Al_2O_3 for the 100 orientation with symmetric Gauss distribution. The full width at half maximum (FWHM) of the rocking curve of PZT//MgO is below 3°, which reveals the strong 100 preferred orientation of the polycrystalline grains. In contrast, the PZT//Al_2O_3 sample presents the very wide FWHM of rocking curve about 11.2°, which indicates the random orientation with the low crystalline distribution of 100 direction.

Several d-spacing of PZT on MgO (e.g., 200, 210 plane) are slightly larger than that of PZT on Al_2O_3. It is due to the similar lattice structure and well-ordered heterogeneous matching of MgO to PZT. In contrast, there are significant differences of crystalline structures between Al_2O_3 and PZT, which have less effect on the d-spacing of PZT. The insets of Figs. 1(b) and 1(c) are the Kikuchi line patterns obtained by

electron backscatter diffraction (EBSD) to compare the two PZT films. The Kikuchi lines of the PZT on the MgO also display a uniformly defined stereographic map with strong [100], [110], and [111] reflector lines induced by the texturing, whereas those on the Al_2O_3 show irregular and high-index patterns such as $[\bar{2}5\bar{4}]$, $[\bar{3}9\bar{7}]$, and $[\bar{1}4\bar{3}]$.

Raman spectroscopy was performed to investigate the phases of the PZT thin films on the two different substrates, as shown in Figs. 1(d) and 1(e). Phase issues are critical factors in piezoelectric properties because the PZT phases directly affect diverse polarization routes. The continuous phase transition and coexistence throughout the MPB region between rhombohedral PZT (r-PZT) and tetragonal PZT (t-PZT) produce the outstanding electromechanical characteristics [34, 42]. Intriguingly, the Raman spectra of each PZT thin film describe different phase tendencies, even though the MPB composition and the deposition condition were completely identical. Figure 1(d) is the spectrum from the PZT film on MgO, designating the coexistence of r-PZT and t-PZT as the standard MPB region (Fig. 1(d)) [43]. On the other hand, Fig. 1(e) exhibits the Raman shift of the PZT film on Al_2O_3 where the bands of the A_1(1LO)+E(2LO), E(2TO), and E+B_1 modes abruptly increase in intensity, showing that t-PZT is superior to r-PZT [43]. In particular, the clear appearance of the A_1(2TO) mode is the unequivocal signature of tetragonal-dominant MPB rather than rhombohedral [44]. The collapsed phase balance into t-PZT is maleficent to piezoelectricity in the MPB composition of the PZT thin films on Al_2O_3. These phasic behaviors of PZT films on MgO and Al_2O_3 are also supported by the glancing (2θ) scan XRD data (Fig. S1 in the ESM), corresponding to peak broadening or splitting. This phase variation in the PZT thin film is not caused by any stoichiometric composition changes, as demonstrated by the energy-dispersive X-ray spectroscopy (EDS) results, which indicate almost the same composition and no chemical reaction in either of the PZT films (Figs. S3 and S4, and Table S1 in the ESM). To additionally investigate the MPB phase balances of each PZT thin film, we performed and analyzed high-resolution fine-scan XRD with {200} peaks [45, 46]. In PZT//MgO, as shown in Fig. S5(a) in the ESM, the rhombohedral phase component is slightly dominant compared to the tetragonal element according to deconvoluted portions. In contrast, the tetragonal component is more predominant than the rhombohedral in PZT//Al_2O_3 (Fig. S5(c) in the ESM), similar to Raman spectroscopy.

As shown in the high-resolution transmission electron microscopy (HRTEM) image of Fig. 1(f), the preferred <100>-oriented PZT lattice is well matched and stitched with the (100) plane of the MgO single-crystalline substrate. The selected area electron diffraction (SAED) patterns in the insets of Fig. 1(f) display the high-lattice coherency between the MgO wafer and the directional-grown PZT thin film. On comparison, the HRTEM images and the SAED patterns in Fig. 1(g) show the sharp flatness of the Al_2O_3 surface and the random orientation of the PZT crystallites, indicating that there is no crystalline relationship between the Al_2O_3 wafer and the deposited PZT film. Interestingly, these TEM and SAED analyses confirm that the crystallinity of the PZT thin film on MgO is also much better than that of PZT on Al_2O_3, resulting in improved PZT piezoelectricity on the MgO substrate. These propensities for crystalline orientation and crystallinity are maintained up to the top parts of each PZT film (Fig. S6 in the ESM). The overall dark-field TEM and the high-resolution backscattered electron (BSE) SEM are also explained in Figs. S7 and S8 in the ESM.

3.3 First-principles calculation of PZT thin-film system

We performed first-principles calculations with density functional theory (DFT) for the PZT thin films on each basal substrate, to not only systemically explain the crystal orientation difference but also fundamentally interpret the phase variation and distinguished crystallinity. The first-principles calculations are based on the Kohn–Sham equation as conducted in the VASP code [28]. The calculation steps are described in our previous studies and in the Experimental section in detail [29, 30, 47–50]. It should be noted that the quantum mechanical calculations for the PZT thin films with MPB composition were applied to the rhombohedral and tetragonal phases, since the thermodynamic restriction about the monoclinic phase is not already severe in the energy

formalism such as order-invariant coefficients [35]. Furthermore, the controversy about monoclinic adaptive states (m_a-, m_b-, and m_c-PZT) can be reasonably negated in the *ab initio* simulation because the monoclinic symmetry (*Cm* or *Pm*) is regarded as the subgroup of both rhombohedral and tetragonal symmetries at nanotwins [42, 51].

The basic structure and formation of the PZT crystals (i.e., r-PZT and t-PZT) were calculated to investigate the PZT thin films on each substrate, as shown in Fig. 2(a). The lattice parameters of r-PZT were calculated to be a = 4.11 Å and α = 89.23° (Fig. 2(a)(1)), whereas those of t-PZT were determined to be a = 4.01 Å and c = 4.16 Å (Fig. 2(a)(2)). These geometric predictions in conventional unit cell systems are almost consistent with previously reported analytical experiments [52, 53]. As recorded in Fig. 2(a), the formation energy (E_{form}) levels of r-PZT and t-PZT were then solved as −7.64 and −7.95 eV per primitive cell (Fig. S9 in the ESM), respectively.

3.4 Interpretation for the control of crystal orientation

To clarify the nature of the PZT thin films on the two different substrates, the interfacial energy (E_γ) levels between the films and substrates were evaluated. As shown in Fig. 2(b), the first-principles modeling identifies the [100] crystalline orientation of the PZT thin films as the most stable configuration on the [100] MgO wafer, in cases of both the coexisting r-PZT and t-PZT. In the r-PZT system, the [100] texturing direction is reasonable with a rhombohedral angle α of nearly 90°, since the lattice parameter a is very similar to that of MgO. In the coexisting t-PZT (Fig. 2(b)(2)), the preferred orientation is not [001] but [100], which means that the c-axis of the tetragonal cell is parallel to the interface with the MgO wafer. It is because the lattice parameter along c-axis (4.16 Å) of t-PZT is closer to the lattice parameter of MgO (4.20 Å) rather than a-axis (4.01 Å) of t-PZT. Thereby, a smaller uniaxial strain is applied on the (100) plane of t-PZT (a- × c-axes) on the (100) plane of MgO than the (001) plane (a- × a-axes). Note that this coexisting t-PZT configuration is advantageous to IDE-type devices, arranged along the c-axis of t-PZT, owing to the high polarization translation in c-axis. Consequently, these crystal orientations of PZT with MPB on the MgO substrate can produce large piezoelectric properties, resulting from the maximized polarization rotation of r-PZT and the maximum translation of t-PZT [34, 54].

On the [0001] Al_2O_3 wafer, in contrast, the calculated E_γ of both the [100]-textured r-PZT and t-PZT films is about ten times higher than that of the MgO wafer, as compared in Figs. 2(b) and 2(c). Not only the [100] orientation but also other higher-index orientations of the PZT are energetically unfavorable on the Al_2O_3 substrate. Therefore, the PZT thin film inevitably forms a random orientation on the Al_2O_3 wafers because there is no matching orientation between the film and the substrate. Even the E_γ of lowest index-textured PZT on Al_2O_3 (0.142 and 0.154 eV·Å^{-2} converted as ~230 and ~250 kJ·mol^{-1}) is much higher than the growth activation energy of the PZT film (~110 kJ·mol^{-1}) calculated by the Avrami method [55].

3.5 Interpretation for the modulation of crystallinity

The degree of crystallinity can also be delineated by the DFT results and the crystallization-free energy. Because the E_γ between PZT and MgO is sufficiently low (Fig. 2(b)), heterogeneous nucleation can occur stably and easily at the crystallographic-coherent interface during PZT crystallization. In the case of PZT on Al_2O_3, however, the nucleation step cannot happen ordinarily at the interface due to the high E_γ between the PZT and Al_2O_3, as shown in Fig. 2(c). Instead, heterogeneous nucleation can arise intermittently at free surfaces, sol–gel polymeric inclusions, or incoherent-interfacial clingers during the PZT crystallization on Al_2O_3; however, the nucleation step is rendered slow and sluggish because all of these sites also have high energy levels, compared to the E_γ of the PZT on MgO (e.g., the free surface energy of PZT thin films ≅ 0.06–0.09 eV·Å^{-2}). Therefore, it is clear that the nucleation events strongly depend upon the underlying interface. As nucleation is the determining step of perovskite formation and the critical step of crystallinity in the entire PZT crystallization mechanism [55, 56], the crystallinity of PZT on Al_2O_3 is poorer than that of PZT on MgO, in accordance with the TEM analyses. The BSE-SEM

images can also imply the nucleation tendencies (Fig. S8 in the ESM).

3.6 Interpretation for the modulation of MPB phase balance

The DFT calculations sequentially explain the phase variation of the PZT thin films according to the basal substrates. On the MgO substrate, the E_γ levels of r-PZT (Fig. 2(b)(1)) and t-PZT (Fig. 2(b)(2)) are almost the same; the energy difference is just 0.0051 eV·Å^{-2} (~8 kJ·mol^{-1}). Hence, the two phases of PZT can easily and naturally coexist as a MPB composition on the MgO wafer due to the slight energy difference. Although there is a subtle energetic predominance of r-PZT caused by the interfacial lattice strain difference, it can be rather beneficial owing to the piezoelectric priority of the <100>-textured rhombohedral phase, as noted in the Raman spectroscopy analyses [16, 57]. Consequently, the well-balanced MPB phase state of the PZT film on MgO induces a synergetic effect for the dramatic increase of piezoelectricity, along with the preferred orientation and excellent crystallinity.

In contrast to the PZT//MgO system, the PZT//Al_2O_3 system cannot utilize the calculated interfacial behaviors with preferred orientation (Fig. 2(c)) to resolve the phase variation phenomenon because of the confirmed random orientation and non-interfacial nucleation. In place of the interfacial variants, the inherent formation (E_{form}) of each PZT phase becomes the main determinant for the PZT phase states on the Al_2O_3 substrate. As shown in Fig. 2(a), there is a considerable difference in E_{form} between r-PZT and t-PZT, of 0.312 eV·cell^{-1} (~30 kJ·mol^{-1}), causing a pseudo-balanced phase state with energetic dominance of t-PZT, despite the MPB composition.

3.7 Interfacial states and polarization

Figures 3(a) and 3(b) depict the DOS at PZT//MgO and PZT//Al_2O_3 interfaces. The differences in E_γ of the PZT films on each substrate are caused by the lattice coherency between PZT and substrates. Since the lattice structures and parameters of the MgO are very analogous to those of the PZT crystals, the DOS at the PZT//MgO interface indicates strong hybridized bonds, as indicated by the aligned DOS ridges (inset of Fig. 3(a)). In contrast, as shown in the misalignments of DOS (inset of Fig. 3(b)), there is no hybridization at the PZT//Al_2O_3 interface, because there are numerous broken and instable dangling bonds. These first-principles DFT calculations for DOS are consistent

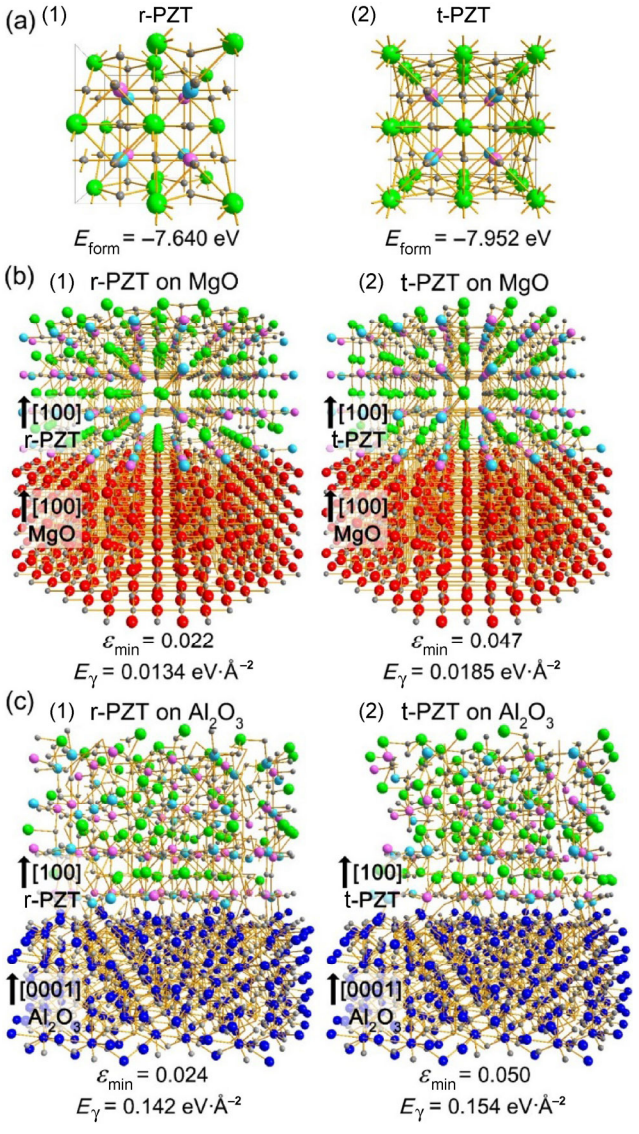

Figure 2 First-principles calculations of rhombohedral and tetragonal PZT thin films on MgO and Al_2O_3. (a) First-principles DFT-calculated conventional cell and formation energy of (1) r-PZT and (2) t-PZT. (b) Calculated crystal structures, bonds, minimized lattice strain, and interfacial energy of [100]-oriented (1) r-PZT and (2) t-PZT on a [100] direction MgO wafer. (c) Calculated crystal structures, bonds, minimized lattice strain, and interfacial energy of [100]-oriented (1) r-PZT and (2) t-PZT on a [0001] direction Al_2O_3 wafer. Each elemental atom is denoted in different colors: Pb—green, Zr—cyan, Ti—pink, O—gray, Mg—red, and Al—blue.

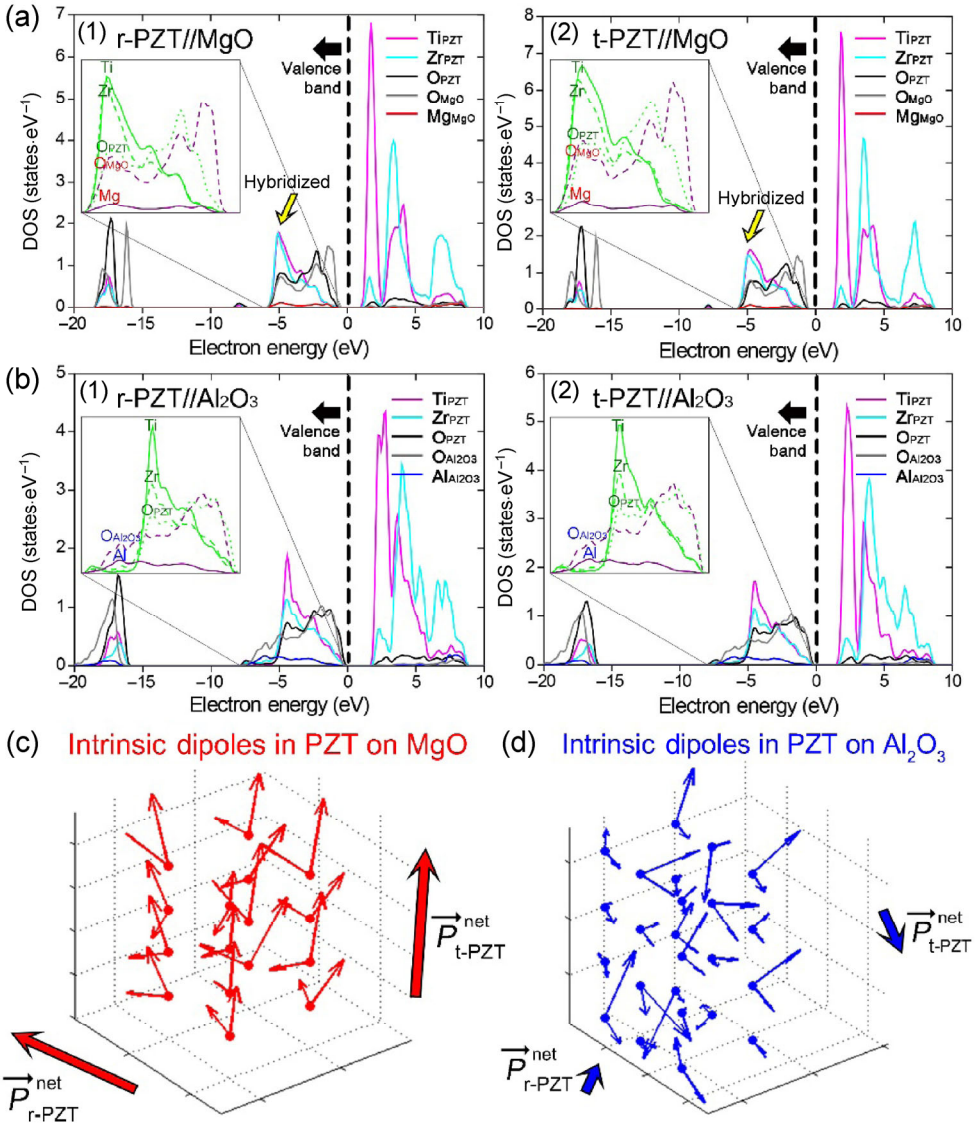

Figure 3 DFT simulations of PZT interfacial states and intrinsic polarizations. (a) Normalized interfacial DOS of (1) r-PZT and (2) t-PZT on MgO. (b) Normalized interfacial DOS of (1) r-PZT and (2) t-PZT on Al_2O_3. Insets: the magnified DOS graphs of outer valence band of each element to show whether they are hybridized. Note that the interfacial calculations were conducted at the Ti, Zr layer of PZT, rather than the Pb layer because the former is more stable than the latter in every interfacial PZT case. 3D quiver plots of simulated intrinsic polarization (before poling) in the MPB-stoichiometric PZT thin films on the (c) MgO and (d) Al_2O_3 substrates. $\vec{P}$ denotes the mean vectors of net intrinsic polarization in each PZT phase, r-PZT and t-PZT.

with the simulated projection schematics (Fig. S10 in the ESM) and the experimental analyses.

Figures 3(c) and 3(d) show the three-dimensional (3D) quiver plots depicting the intrinsic polarization based on the atomic displacement and born effective charge in the PZT films with MPB composition on MgO and Al_2O_3, respectively. Although the inherent polarization does not directly affect macroscopic piezoelectric signals due to the disordered domain alignment before poling, it is highly essential to enhance piezoelectricity resulting from the easy dipole alignment that occurred during the poling process. The dipole moments of the PZT on MgO are larger and more ordered than those of PZT on Al_2O_3.

As a result, the well-defined intrinsic polarization of the PZT film on MgO enhances poling effects, mitigates piezoelectric aging problems, and stands robustly against depolarization [13], compared to

the case of the Al_2O_3 substrate. The partial loss of ferroelectric nature in the PZT film on Al_2O_3 is presumably due to the drastic distortions of the perovskite structure caused by the interfacial instability.

3.8 Flexible crystallographic-controlled PZT thin film

Figure 4(a) shows the flexible energy harvester using the highly optimized PZT thin film based on thorough theoretical atomic investigations. The crystallographic-controlled PZT film prepared on MgO was successfully transferred onto a flexible PET sheet without material failure even during laser irradiation (i.e., inorganic-based laser lift-off, ILLO), which is similar to the conventional case of the non-controlled PZT film on Al_2O_3 (Fig. 4(b)). In the ILLO process, a 308 nm-wavelength XeCl pulsed laser (duration time ~30 ns) penetrates each wafer from the backside since the laser photonic energy (4.02 eV) is much smaller than the substrate band gap energy levels (7–10 eV).

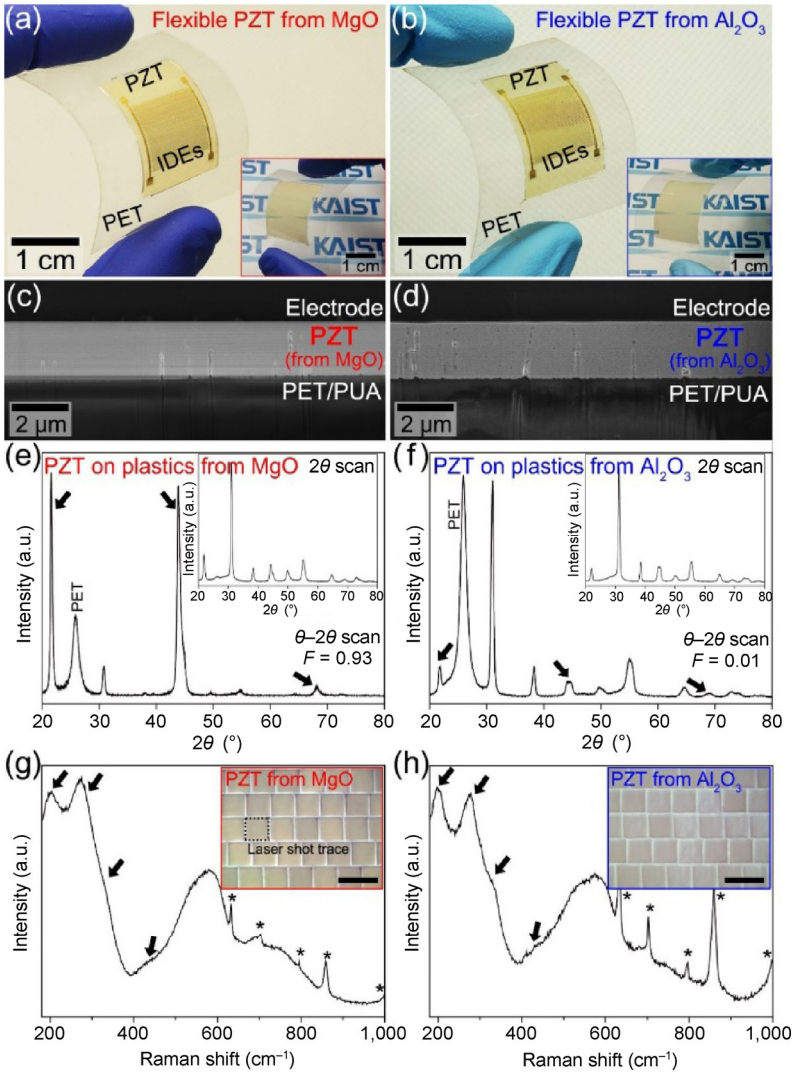

Figure 4 PZT thin-film energy harvesters from (a) the MgO wafer and (b) the Al_2O_3 wafer. Insets: as-transferred PZT thin films on PET substrates using the ILLO processes. Cross-sectional high-resolution SEM images of FIB-cut flexible PZT films from (c) the MgO wafer and (d) the Al_2O_3 wafer. Some pores of the PZT thin films shown in the SEM images are induced by the ion-cutting damage. (e) and (f) θ–2θ scan and 2θ scan (insets) XRD of PZT thin films from the MgO and the Al_2O_3, respectively. (g) and (h) Raman spectra of each PZT thin film from the MgO wafer and the Al_2O_3 wafer. Some peaks from the PET substrates are marked as asterisks. Insets: optical microscopy images of each PZT film surface from MgO and Al_2O_3 wafers after ILLO transfer processing. Scale bars, 1 mm. The black arrows are important XRD peaks or Raman shift bands for the comparison with Fig. 1.

Consequently, the PZT thin film completely absorbs the laser energy at the interface with the substrates, followed by partial melting and dissociation of the PZT because the band gap energy of PZT (3.2–3.6 eV) is lower than the photonic energy of XeCl laser. A detailed report about the fabrication of the flexible thin-film energy harvester and the mechanism of ILLO has been described in our previous reports [7, 8].

Figures 4(c) and 4(d) are focused ion beam (FIB) SEM cross-sectional images of the flexible PZT thin films on PET, transferred from the MgO and Al_2O_3 wafers, respectively. The θ–2θ XRD of Fig. 4(e) shows the preferred orientation of the flexible PZT film from MgO, whereas Fig. 4(f) displays the random orientation of the flexible PZT film from Al_2O_3. Quantitatively, the orientation factors F of each PZT film are almost retained as 0.93 and 0.01, respectively.

As presented in Figs. 4(g) and 4(h), the Raman spectra of the flexible PZT film from MgO and Al_2O_3 indicate that each phase tendency was maintained, even after ILLO. The glancing XRD data additionally show the trends of phases and the differences in crystallinity (the inset of Figs. 4(e) and 4(f)). Notwithstanding these differences in crystallographic characteristics between the two different PZT thin films, the laser-shot interactions of each surface were similar after the ILLO process, as shown in the insets of Figs. 4(g) and (h). Note that strain relaxation during LLO transferring cannot be a meaningful effect on the crystalline system of μm-scale PZT films because the epitaxial strain can be already spontaneously relaxed under a few dozen nm-scale thickness even before the transferring [58, 59]. In addition, grain boundaries of polycrystalline film easily cause and contribute to the strain relaxation before the transferring.

The high-resolution narrow-scan XRD showed also similar phase tendencies even after LLO transferring (Figs. S5(b) and S5(d) in the ESM) despite the minor deviation of the PZT from Al_2O_3. This variation seems to be related to slightly increasing (200) tetragonal trace [45, 46] of the exposed underlying PZT surface. It could be caused due to some diffuse and minor symmetries in MPB such as twin-induced monoclinic and intermediate pseudocubic, which are presumably from intrinsic dynamics of PZT [42] with the incoherent and instable interface against Al_2O_3 as expected in the *ab initio* calculations.

3.9 Finite element method analysis of flexible PZT

Figure 5(a) illustrates the piezopotential of the energy harvester of each PZT film simulated using the finite element method (FEM) by COMSOL software. To predict the internal potential in the bending-stressed condition, we constructed a simplified model consisting of a 2-μm-thick PZT layer with an IDE gap of 100 μm. The FEM simulation was based on the measured relative permittivity and piezoelectric response (Fig. 5(b)) as well as some default physics of COMSOL such as density of PZT. The applied strain can be calculated by the thicknesses of the device layers as ~0.29% at a bending radius of ~2 cm. As expected by the obtained and applied constants (Fig. 5(b)), the PZT thin film from MgO can generate about two times higher piezoelectric potential (Fig. 5(a)(1)) than that from Al_2O_3 (Fig. 5(a)(2)).

3.10 Characterization of crystallographic-modulated flexible energy harvester

To evaluate the ferroelectric characteristics of the PZT thin films, the dielectric constants and losses were measured, as shown in Fig. 5(b). The dielectric properties of the flexible PZT energy harvesters were examined with an oscillation voltage of 5 mV and a frequency range of 1–100 kHz. The dielectric constants of the PZT films from MgO and Al_2O_3 were estimated to be 2,700–2,800 and 2,400–2,500, respectively. Both PZT thin films also showed a very low dielectric loss tangent δ (<0.03). The large dielectric permittivity and small loss factors of both films, from the MgO and Al_2O_3 substrates, manifest the high quality of dense PZT thin films with low defect level. The higher dielectric constant of the flexible PZT from MgO compared to that from Al_2O_3 is due to its more ordered intrinsic ferroelectric polarization. The piezoelectric responses of each PZT thin film were evaluated by measuring their field-dependent piezoelectric coefficient d_{33}, as shown in the inset of Fig. 5(b). The maximum piezocoefficient of the PZT thin film from MgO is about 210 pm·V^{-1}, whereas the maximum piezocoefficient of the PZT film from

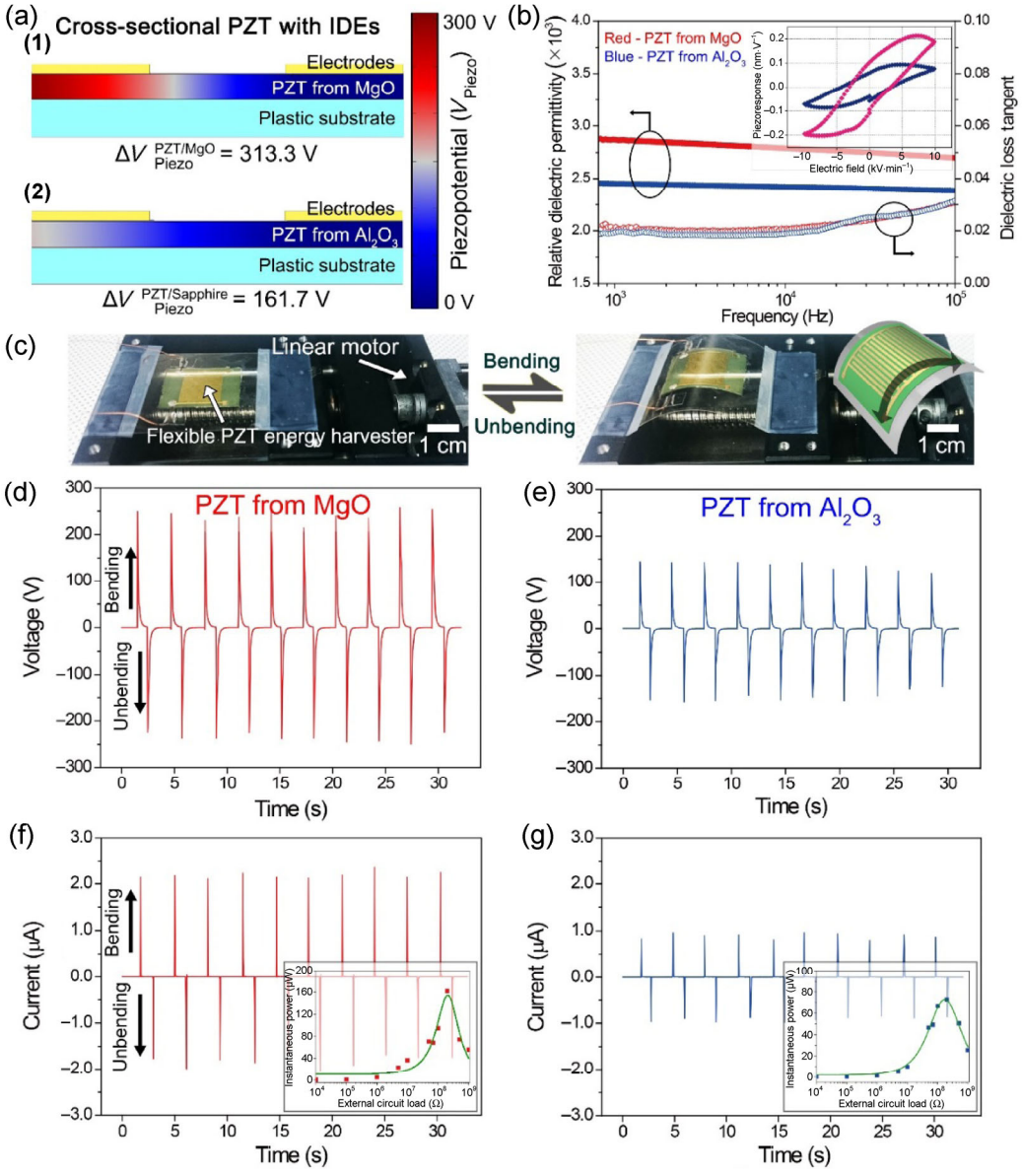

Figure 5 Characterization of crystallographic-controlled flexible PZT energy harvester. (a) Using FEM-based COMSOL multiphysics, simulated piezopotential in each PZT thin film with IDEs, (1) the transferred PZT films from MgO and (2) from Al_2O_3. (b) Dielectric constants, losses, and (inset) piezoresponses of each PZT thin film. The degraded piezoresponse at zero field in the hysteresis is presumably due to the significant dielectric interference by PUA adhesion and the high sheet resistance of ITO for a sandwich-type measuring electrode structure, combined with the short biasing time of analyzer. (c) Bending and unbending motions of the flexible energy harvester devices by a linear motor. The right inset shows the appropriate bending direction which is perpendicular to IDE fingers. (d)–(g) During mechanical stimulations, the produced voltage and current from (d) and (f) the flexible PZT thin-film generator made from the MgO wafer and (e) and (g) the flexible PZT thin-film generator from the Al_2O_3 wafer, respectively. Insets: instantaneous output power levels of each PZT thin-film energy harvester, as a function of the external load resistance.

Al_2O_3 is just about 90 pm·V^{-1} at the poling field of 100 kV·cm^{-1}, verifying that the controlled PZT has more than two times higher piezoelectricity than the non-controlled PZT. These values are considered as reasonable results because they correspond to previously reported analyses [8, 19, 60, 61]. We also measured the polarization versus electric field (*P*–*E*) hysteresis curves to show that the remnant and rising polarization of PZT film device from MgO is larger than that of the PZT device from Al_2O_3

(Fig. S12 in the ESM).

For piezoelectric materials, the piezoelectric coefficient (d) can be described as

$$d \sim Q\varepsilon_0\chi_r P \quad (4)$$

where Q is the electrostrictive constant; ε_0 is the vacuum permittivity; χ_r is the relative permittivity; and P is the polarization along the polarity induced by the electric field [34]. Since the polarization is large in the controlled PZT thin film on MgO due to the well-aligned ferroelectric domains and intrinsic polarized direction, the piezocoefficient can be much higher than that of non-controlled PZT film on Al_2O_3. To investigate the poling efficiency, the impedance and phase angle were additionally evaluated (Fig. S13 in the ESM). Note that the high piezoelectric constants are regarded as a representative figure of merit for microelectromechanical system (MEMS) applications such as sensors, transducers, and energy harvesters.

Figure 5(c) displays the mechanical deformation of the flexible energy harvesters while generating voltage and current: bending and unbending states. The working principle of IDE-type flexible energy harvesters is characterized by the repeated piezoelectric effect between adjacent electrodes (see the ESM) [7, 62]. The flexible PZT thin-film energy harvester made from the MgO wafer produced an open-circuit voltage of ~250 V and a short-circuit current of ~2.3 μA, whereas the flexible PZT thin-film energy harvester made from the Al_2O_3 substrate generated ~150 V and ~0.9 μA with a bending strain of 0.29% (Figs. 5(d)–5(g), switching polarity tests in Fig. S14 in the ESM). As anticipated by the piezocoefficients, the current of the PZT energy harvester from MgO is more than two times higher than that of the PZT generator from Al_2O_3, because the induced current charge (q) is directly proportional to d_{ij} as shown below

$$q = A\sigma d_{ij} \quad (5)$$

where A is the surface area of piezoelectric region and σ is the stress on the region. The generated voltage (V) of the PZT generator from MgO is less than two times larger than that from Al_2O_3, probably due to the somewhat higher dielectric constant (k) of the PZT thin film from MgO, as expressed in the equation below

$$V = l\sigma g_{ij} = l\sigma\frac{d_{ij}}{k\varepsilon_0} \quad (6)$$

where l is the distance between electrodes and g_{ij} is the piezoelectric voltage constant. In contrast to the proper bending direction perpendicular to the fingers of IDEs, the parallel bending cannot generate good output because piezoelectric potential cannot be generated well between the fingers of IDEs (Fig. S15 in the ESM). The maximum instantaneous power of the flexible PZT thin-film energy harvesters from MgO and Al_2O_3 were ~160 and ~75 μW at the circuital load of ~100 MΩ, respectively, as compared in the insets of Figs. 5(f) and 5(g). The external circuit load values at the maximum power for both PZT film energy harvesters are almost same because their internal electric impedances (Fig. S13 in the ESM) are also almost same. It is because of the very high resistance (>200 GΩ, out of measurement limit) of a pair of IDEs (impedance (Z) is indicated as R + jX, where R is resistance, and X is reactance which is affected by capacitance and inductance). Moreover, it should be noted that the dielectric constants are already similarly high compared to their difference.

The resultant voltage and volumetric current density (covering not only the area but also the thickness of the piezoelectric film) of this flexible PZT energy harvester from MgO (250 V and 4.88 mA·cm^{-3}) were, respectively, 556% and 503% higher than those of a flexible $PbMg_{1/3}Nb_{2/3}O_3$–$PbZr_{1-x}Ti_xO_3$ (PMN–PZT) single-crystalline generator (45 V and 0.97 mA·cm^{-3}, respectively) with the same IDE design [10]. The PMN–PZT used in the previous report was grown by a solid-state single-crystal growth (SSCG) method [15] and not using molten ceramic-based ingot growth. Moreover, the volumetric power density is even 822% larger than the previous report (356 mW·cm^{-3} vs. 43.3 mW·cm^{-3}). This controlled polycrystalline PZT thin film can overcome the demerits of single-crystalline piezoceramic films, such as the thinning-induced piezoelectric malfunction and the domain clamping-based degradation [9, 11, 14]. It should be noted that MIM-structured flexible energy harvesters cannot be compared with IDE types because they have entirely

different device structures and other piezoelectric modes [7, 9].

3.11 Tiny vibrational energy harvesting in a real traffic system

Tiny vibrations are the most common and continuous mechanical energy sources in our ambient environments, compared with large bending kinetics; for example, persistent oscillation, agitation, and sway always exist in social traffic systems such as roads, railways, flights, and vessels. To scavenge this small-scale and low-frequency vibration energy, flexible energy harvesters with high performance and light volume could be established in these transportation systems. However, the tiny vibration-based flexible energy harvester has been rarely studied yet, because it is difficult to realize sufficient output and the required responsive characteristics of energy harvesting relative to the nearly imperceptible vibrations (acceleration < 0.1 g, displacement < 5 mm). In this study, we applied the highly efficient and flexible PZT thin-film energy harvester to a traffic system programmed from a real highway bridge (Yeondae Bridge, Fig. S16 in the ESM and Experimental section), which may be used in fatigue-crack sensors [63]. When some vehicles pass through the bridge, irregular vibrations occur with aftershocks, as illustrated in Fig. 6(a). Using a commercial module consisting of complex sensors and arbitrary waveform generators for civil engineering, the tiny traffic vibrations can be applied to our flexible energy harvesters on a laboratory scale, i.e., Infrastructure-On-a-Lab, as reported in our previous research (Fig. 6(b)) [64].

In the case of vibration by a truck, the maximum generated voltage signal of the flexible PZT film generator from MgO was ~4 V (Fig. 6(c)). In contrast, the voltage of the PZT energy harvester from Al_2O_3 was just about 1.5 V (Fig. 6(d)). The voltage levels produced by the vibrations decrease sequentially as the passing vehicles become smaller, i.e., a bus, a recreational vehicle (RV), and a sedan. The generated output signals gradually disappear during the aftershocks, indicating the excellent flexibility of our energy harvesters. Because the turn-on voltage of a commercial blue LED chip is ~2.5 V, only the flexible PZT from MgO can induce a flicker of LED lighting, unlike the device from Al_2O_3, as captured in the insets of Figs. 6(c) and 6(d). The vibration-generated current was also measured using the traffic vibrations from

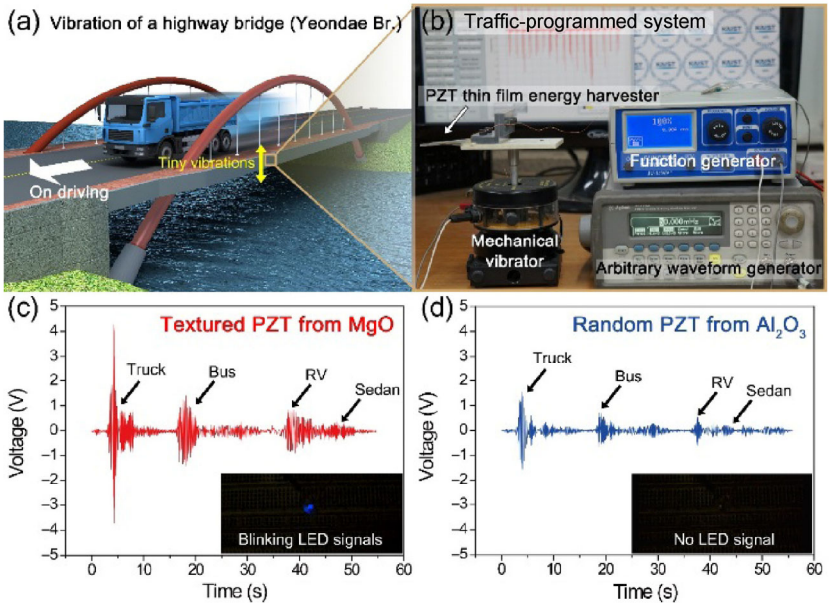

Figure 6 Tiny vibrational energy being generated at a real traffic-programmed system. (a) Schematic illustration of traffic vibrations by a vehicle on the highway bridge, which is programmed for our vibrational energy-harvesting test. (b) Picture of traffic-programmed vibration system with the clipped energy harvester. During the traffic vibrations triggered by a truck, a bus, and a RV car, the generated voltage signals of the PZT film energy harvesters made from (c) the MgO and (d) Al_2O_3 substrates. Insets show that only the flexible PZT thin-film energy harvester from MgO can turn on the blue LED bulbs.

random vehicles (Fig. S17 in the ESM). This result is the first demonstration of a flexible piezoelectric energy harvester for arbitrary and tiny vibrations in a real traffic system. Furthermore, it strongly proves that atomic-scale modifications can affect various macroscale applications, such as massive constructions. We are currently developing low-frequency mechanical resonance [65] and stacked flexible modules for the time-displacement amplification of vibrational energy harvesting in some large-scale infrastructures, e.g., Incheon Airport Grand Bridge.

4 Conclusions

We investigated the crystallographic control of PZT thin films with MPB composition via substrative modulation, from fundamental atomic-scale materials science to practical-scale energy harvesting applications. When the PZT thin film was deposited on a lattice-coherent substrate (i.e., MgO), the preferred orientations, the balanced phases, and the notable crystallinity can be achieved for high piezoelectricity, in contrast to the PZT film on a sapphire (Al_2O_3) wafer. To understand the phenomenological behaviors in the PZT films of MPB, we utilized DFT calculations to understand the mechanisms of crystallographic orientations, phase variations, and crystallinity. Based on the theoretical interpretation, a high-performance flexible piezoelectric energy harvester was successfully fabricated on plastics using a crystallographic-controlled PZT thin film from the MgO substrate by the ILLO transfer process. The flexible controlled PZT device exhibited higher voltage, current density, and power density than even the previously reported flexible single-crystalline film generator, by 556%, 503%, and 822%, respectively. Energy harvesting of tiny vibrations in a traffic system was realized using the high-output flexible PZT energy harvester at a bridge-programmed stage, which has not been demonstrated so far. This study paves the way to a fundamental understanding about atomic-scale material systems, and consequently provides opportunities to modify or enhance macroscale infrastructural applications. Our tiny-vibration harvester can also provide a complementary solution to conventional heavy-weight and bulky-volume electromagnetic devices.

Acknowledgements

The authors would like to thank the CEO of RoboPrint Co., Jung Gyu Park. This study was backed up by the research project–Product Development of Wearable Self-Powered Energy Device and Integrated Self-Powered Energy Device from PEPS (No. G01150219). This research was supported by Nano·Material Technology Development Program through the National Research Foundation of Korea (NRF) funded by the Ministry of Science, ICT and Future Planning (MSIP) (No. 2016M3A7B4910636). This is also supported by Global Frontier R&D Program on Center for Integrated Smart Sensors (No. CISS-2016M3A6A6929958) funded by MSIP through NRF of Korea government. This work was additionally supported by Basic Science Research Program through the NRF of Korea funded by MSIP (No. 2016R1A2B4010674).

Electronic Supplementary Material: Supplementary material (experiments with additional interpretations, XRD, EDS, HRTEM, SEM, measurement data, photograph pictures, etc.) is available in the online version of this article at http://dx.doi.org/10.1007/s12274-016-1304-6.

References

[1] Hinchet, R.; Kim, S. W. Wearable and implantable mechanical energy harvesters for self-powered biomedical systems. *ACS Nano* **2015**, *9*, 7742–7745.

[2] Wang, X. D. Piezoelectric nanogenerators—Harvesting ambient mechanical energy at the nanometer scale. *Nano Energy* **2012**, *1*, 13–24.

[3] Larcher, L.; Roy, S.; Mallick, D.; Podder, P.; de Vittorio, M.; Todaro, T.; Guido, F.; Bertacchini, A.; Hinchet, R.; Keraudy, J. et al. Vibrational energy harvesting. In *Beyond-CMOS Nanodevices 1*; Balestra, F., Ed.; John Wiley & Sons, Inc.: Hoboken, NJ, USA, 2014.

[4] Wang, Z. L. Energy harvesting for self-powered nanosystems. *Nano Res*. **2008**, *1*, 1–8.

[5] Hwang, G.-T.; Byun, M.; Jeong, C. K.; Lee, K. J. Flexible piezoelectric thin-film energy harvesters and nanosensors for biomedical applications. *Adv*. *Healthcare Mater*. **2015**, *4*, 646–658.

[6] Dagdeviren, C.; Shi, Y.; Joe, P.; Ghaffari, R.; Balooch, G.; Usgaonkar, K.; Gur, O.; Tran, P. L.; Crosby, J. R.; Meyer,

M. et al. Conformal piezoelectric systems for clinical and experimental characterization of soft tissue biomechanics. *Nat. Mater.* **2015**, *14*, 728–736.

[7] Park, K. I.; Son, J. H.; Hwang, G. T.; Jeong, C. K.; Ryu, J.; Koo, M.; Choi, I.; Lee, S. H.; Byun, M.; Wang, Z. L. et al. Highly-efficient, flexible piezoelectric PZT thin film nanogenerator on plastic substrates. *Adv. Mater.* **2014**, *26*, 2514–2520.

[8] Jeong, C. K.; Park, K.-I.; Son, J. H.; Hwang, G.-T.; Lee, S. H.; Park, D. Y.; Lee, H. E.; Lee, H. K.; Byun, M.; Lee, K. J. Self-powered fully-flexible light-emitting system enabled by flexible energy harvester. *Energy Environ. Sci.* **2014**, *7*, 4035–4043.

[9] Hwang, G. T.; Park, H.; Lee, J. H.; Oh, S.; Park, K. I.; Byun, M.; Park, H.; Ahn, G.; Jeong, C. K.; No, K. et al. Self-powered cardiac pacemaker enabled by flexible single crystalline PMN-PT piezoelectric energy harvester. *Adv. Mater.* **2014**, *26*, 4880–4887.

[10] Hwang, G.-T.; Yang, J.; Yang, S. H.; Lee, H.-Y.; Lee, M.; Park, D. Y.; Han, J. H.; Lee, S. J.; Jeong, C. K.; Kim, J. et al. A reconfigurable rectified flexible energy harvester via solid-state single crystal grown PMN-PZT. *Adv. Energy Mater.* **2015**, *5*, 1500051.

[11] Hwang, G.-T.; Kim, Y.; Lee, J.-H.; Oh, S.; Jeong, C. K.; Park, D. Y.; Ryu, J.; Kwon, H.; Lee, S.-G.; Joung, B. et al. Self-powered deep brain stimulation via a flexible PIMNT energy harvester. *Energy Environ. Sci.* **2015**, *8*, 2677–2684.

[12] Jeong, C. K.; Lee, J.; Han, S.; Ryu, J.; Hwang, G.-T.; Park, D. Y.; Park, J. H.; Lee, S. S.; Byun, M.; Ko, S. H. et al. A hyper-stretchable elastic-composite energy harvester. *Adv. Mater.* **2015**, *27*, 2866–2875.

[13] Baek, S. H.; Park, J.; Kim, D. M.; Aksyuk, V. A.; Das, R. R.; Bu, S. D.; Felker, D. A.; Lettieri, J.; Vaithyanathan, V.; Bharadwaja, S. S. N. et al. Giant piezoelectricity on si for hyperactive MEMS. *Science* **2011**, *334*, 958–961.

[14] Lee, H. J.; Zhang, S. J.; Luo, J.; Li, F.; Shrout, T. R. Thickness-dependent properties of relaxor-$PbTiO_3$ ferroelectrics for ultrasonic transducers. *Adv. Funct. Mater.* **2010**, *20*, 3154–3162.

[15] Kang, S.-J. L.; Park, J.-H.; Ko, S.-Y.; Lee, H.-Y. Solid-state conversion of single crystals: The principle and the state-of-the-art. *J. Am. Ceram. Soc.* **2015**, *98*, 347–360.

[16] Du, X. H.; Zheng, J. H.; Belegundu, U.; Uchino, K. Crystal orientation dependence of piezoelectric properties of lead zirconate titanate near the morphotropic phase boundary. *Appl. Phys. Lett.* **1998**, *72*, 2421–2423.

[17] Taylor, D. V.; Damjanovic, D. Piezoelectric properties of rhombohedral Pb(Zr, Ti)O_3 thin films with (100), (111), and "random" crystallographic orientation. *Appl. Phys. Lett.* **2000**, *76*, 1615–1617.

[18] Park, C.-S.; Kim, S.-W.; Park, G.-T.; Choi, J.-J.; Kim, H.-E. Orientation control of lead zirconate titanate film by combination of sol-gel and sputtering deposition. *J. Mater. Res.* **2005**, *20*, 243–246.

[19] Qi, Y.; Jafferis, N. T.; Lyons, K., Jr.; Lee, C. M.; Ahmad, H.; McAlpine, M. C. Piezoelectric ribbons printed onto rubber for flexible energy conversion. *Nano Lett.* **2010**, *10*, 524–525.

[20] Brooks, K. G.; Reaney, I. M.; Klissurska, R.; Huang, Y.; Bursill, L.; Setter, N. Orientation of rapid thermally annealed lead zirconate titanate thin films on (111) Pt substrates. *J. Mater. Res.* **1994**, *9*, 2540–2553.

[21] Kalpat, S.; Uchino, K. Highly oriented lead zirconium titanate thin films: Growth, control of texture, and its effect on dielectric properties. *J. Appl. Phys.* **2001**, *90*, 2703–2710.

[22] Qin, H. X.; Zhu, J. S.; Jin, Z. Q.; Wang, Y. PZT thin films with preferred-orientation induced by external stress. *Thin Solid Films* **2000**, *379*, 72–75.

[23] Cattan, E.; Velu, G.; Jaber, B.; Remiens, D.; Thierry, B. Structure control of Pb(Zr, Ti)O_3 films using $PbTiO_3$ buffer layers produced by magnetron sputtering. *Appl. Phys. Lett.* **1997**, *70*, 1718–1720.

[24] Park, C.-H.; Son, Y.-G.; Won, M.-S. Microstructure and ferroelectric properties of r. f. magnetron sputtering derived PZT thin films deposited on interlayer (PbO/TiO_2). *Microchem. J.* **2005**, *80*, 201–206.

[25] Yeager, C. B.; Trolier-McKinstry, S. Epitaxial Pb(Zr_x, Ti_{1-x})O_3 ($0.30 \leqslant x \leqslant 0.63$) films on (100)MgO substrates for energy harvesting applications. *J. Appl. Phys.* **2012**, *112*, 074107.

[26] Budd, K. D.; Dey, S. Y.; Payne, D. A. Sol-gel processing of $PbTiO_3$, $PbZrO_3$, PZT, and PLZT thin films. *Br. Ceram. Proc.* **1985**, *36*, 107–121.

[27] Chen, S.-Y.; Chen, I.-W. Texture development, microstructure evolution, and crystallization of chemically derived PZT thin films. *J. Am. Ceram. Soc.* **2005**, *81*, 97–105.

[28] Kresse, G.; Furthmüller, J. Efficient iterative schemes for *ab initio* total-energy calculations using a plane-wave basis set. *Phys. Rev. B* **1996**, *54*, 11169–11186.

[29] Blöchl, P. E. Projector augmented-wave method. *Phys. Rev. B* **1994**, *50*, 17953–17979.

[30] Perdew, J. P.; Burke, K.; Ernzerhof, M. Generalized gradient approximation made simple. *Phys. Rev. Lett.* **1996**, *77*, 3865–3868.

[31] Monkhorst, H. J.; Pack, J. D. Special points for brillouin-zone integrations. *Phys. Rev. B* **1976**, *13*, 5188–5192.

[32] Batirev, I. G.; Alavi, A.; Finnis, M. W. Equilibrium and adhesion of Nb/sapphire: The effect of oxygen partial pressure. *Phys. Rev. B* **2000**, *62*, 4698–4706.

[33] Liu, L. M.; Wang, S. Q.; Ye, H. Q. First-principles study of polar Al/TiN(111) interfaces. *Acta Mater.* **2004**, *52*, 3681–3688.

[34] Damjanovic, D. Contributions to the piezoelectric effect in ferroelectric single crystals and ceramics. *J. Am. Ceram. Soc*. **2005**, *88*, 2663–2676.

[35] Ibrahim, A.-B. M. A.; Murgan, R.; Abd Rahman, M. K.; Osman, J. Morphotropic phase boundary in ferroelectric materials. In *Ferroelectrics - Physical Effects*; Lallart, M., Ed.; InTech: Rijeka, Croatia, 2011.

[36] Takayama, R.; Tomita, Y. Preparation of epitaxial $Pb(Zr_xTi_{1-x})O_3$ thin films and their crystallographic, pyroelectric, and ferroelectric properties. *J. Appl. Phys*. **1989**, *65*, 1666–1670.

[37] Adachi, M.; Matsuzaki, T.; Yamada, T.; Shiosaki, T.; Kawabata, A. Sputter-deposition of [111]-axis oriented rhombohedral PZT films and their dielectric, ferroelectric and pyroelectric properties. *Jpn. J. Appl. Phys*. **1987**, *26*, 550–553.

[38] Morimoto, K.; Kanno, I.; Wasa, K.; Kotera, H. High-efficiency piezoelectric energy harvesters of *c*-axis-oriented epitaxial PZT films transferred onto stainless steel cantilevers. *Sensor. Actuat. A Phys*. **2010**, *163*, 428–432.

[39] Lotgering, F. K. Topotactical reactions with ferrimagnetic oxides having hexagonal crystal structures—I. *J. Inorg. Nucl. Chem*. **1959**, *9*, 113–123.

[40] Cao, L. Z.; Fu, W. Y.; Wang, S. F.; Wang, Q.; Sun, Z. H.; Yang, H.; Cheng, B. L.; Wang, H.; Zhou, Y. L. Effects of film thickness and preferred orientation on the dielectric properties of $(Bi_{1.5}Zn_{0.5})(Zn_{0.5}Nb_{1.5})O_7$ films. *J. Phys. D: Appl. Phys*. **2007**, *40*, 2906–2910.

[41] Li, W. L.; Zhang, T. D.; Xu, D.; Hou, Y. F.; Cao, W. P.; Fei, W. D. $LaNiO_3$ seed layer induced enhancement of piezoelectric properties in (100)-oriented (1-*x*)BZT-*x*BCT thin films. *J. Eur. Ceram. Soc*. **2015**, *35*, 2041–2049.

[42] Zhang, Y.; Xue, D. Z.; Wu, H. J.; Ding, X. D.; Lookman, T.; Ren, X. B. Adaptive ferroelectric state at morphotropic phase boundary: Coexisting tetragonal and rhombohedral phases. *Acta Mater*. **2014**, *71*, 176–184.

[43] Souza Filho, A. G.; Lima, K. C. V.; Ayala, A. P.; Guedes, I.; Freire, P. T. C.; Melo, F. E. A.; Mendes Filho, J.; Araújo, E. B.; Eiras, J. A. Raman scattering study of the $PbZr_{1-x}Ti_xO_3$ system: Rhombohedral-monoclinic-tetragonal phase transitions. *Phys. Rev. B* **2002**, *66*, 132107.

[44] Camargo, E. R.; Frantti, J.; Kakihana, M. Low-temperature chemical synthesis of lead zirconate titanate (PZT) powders free from halides and organics. *J. Mater. Chem*. **2001**, *11*, 1875–1879.

[45] Kühnlein, T.; Stiegelschmitt, A.; Roosen, A.; Rauscher, M. Microstructure development of PZT ceramics by doping with small amounts of Al_2O_3, SiO_2, and Fe_2O_3. *J. Am. Ceram. Soc*. **2014**, *97*, 1638–1644.

[46] Durruthy-Rodríguez, M. D.; Yáñez-Limón, J. M. Photo-luminescence in doped PZT ferroelectric ceramic system. In *Ferroelectrics - Physical Effects*; Lallart, M., Ed.; InTech: Rijeka, Croatia, 2011.

[47] Cho, S. B.; Chung, Y. C. Spin-polarized bandgap of graphene induced by alternative chemisorption with MgO (111) substrate. *Carbon* **2014**, *77*, 208–214.

[48] Cho, S. B.; Chung, Y.-C. Bandgap engineering of graphene by corrugation on lattice-mismatched MgO (111). *J. Mater. Chem. C* **2013**, *1*, 1595–1600.

[49] Cho, S. B.; Yun, K. H.; Yoo, D. S.; Ahn, K.; Chung, Y. C. Work function tuning of an ultrathin MgO film on an Ag substrate by generating oxygen impurities at the interface. *Thin Solid Films* **2013**, *544*, 541–544.

[50] Cho, S. B.; Lee, S.; Chung, Y.-C. Water trapping at the graphene/Al_2O_3 interface. *Jpn. J. Appl. Phys*. **2013**, *52*, 06GD09.

[51] Jin, Y. M.; Wang, Y. U.; Khachaturyan, A. G.; Li, J. F.; Viehland, D. Conformal miniaturization of domains with low domain-wall energy: Monoclinic ferroelectric states near the morphotropic phase boundaries. *Phys. Rev. Lett*. **2003**, *91*, 197601.

[52] Chentir, M.-T.; Morioka, H.; Ehara, Y.; Saito, K.; Yokoyama, S.; Oikawa, T.; Funakubo, H. Changes of crystal structure and electrical properties with film thickness and Zr/(Zr+Ti) ratio for epitaxial Pb(Zr, Ti)O_3 films grown on (100)c$SrRuO_3$//(100)$SrTiO_3$ substrates by metalorganic chemical vapor deposition. In *Ferroelectrics-Characterization and Modeling*. Lallart, M., Ed.; InTech: Rijeka, Croatia, 2011; pp. 229–244.

[53] Boldyreva, K.; Pintilie, L.; Lotnyk, A.; Misirlioglu, I. B.; Alexe, M.; Hesse, D. Ferroelectric/antiferroelectric $Pb(Zr_{0.8}Ti_{0.2})O_3/PbZrO_3$ epitaxial multilayers: Growth and thickness-dependent properties. *Ferroelectrics* **2008**, *370*, 140–146.

[54] Du, X. H.; Belegundu, U.; Uchino, K. Crystal orientation dependence of piezoelectric properties in lead zirconate titanate: Theoretical expectation for thin films. *Jpn. J. Appl. Phys*. **1997**, *36*, 5580–5587.

[55] Kwok, C. K.; Desu, S. B. *Ceramic Transactions: Ferroelectric Films (Volume 25)*; The American Ceramic Society: Westerville, OH, USA, 1992.

[56] Kwok, C. K.; Desu, S. B. Low temperature perovskite formation of lead zirconate titanate thin films by a seeding process. *J. Mater. Res*. **1993**, *8*, 339–344.

[57] Park, S.-E.; Shrout, T. R. Ultrahigh strain and piezoelectric behavior in relaxor based ferroelectric single crystals. *J. Appl. Phys*. **1997**, *82*, 1804–1811.

[58] Lee, H. N.; Nakhmanson, S. M.; Chisholm, M. F.; Christen, H. M.; Rabe, K. M.; Vanderbilt, D. Suppressed dependence of polarization on epitaxial strain in highly polar ferroelectrics. *Phys*. *Rev*. *Lett*. **2007**, *98*, 217602.

[59] Khan, A. I.; Yu, P.; Trassin, M.; Lee, M. J.; You, L.; Salahuddin, S. The effects of strain relaxation on the dielectric properties of epitaxial ferroelectric $Pb(Zr_{0.2}Ti_{0.8})TiO_3$ thin films. *Appl*. *Phys*. *Lett*. **2014**, *105*, 022903.

[60] Park, C.-S.; Lee, J.-W.; Park, G.-T.; Kim, H.-E.; Choi, J.-J. Microstructural evolution and piezoelectric properties of thick Pb(Zr, Ti)O_3 films deposited by the multi-sputtering method: Part II. Piezoelectric properties. *J*. *Mater*. *Res*. **2007**, *22*, 1373–1377.

[61] Park, G. T.; Choi, J. J.; Ryu, J.; Fan, H. Q.; Kim, H. E. Measurement of piezoelectric coefficients of lead zirconate titanate thin films by strain-monitoring pneumatic loading method. *Appl*. *Phys*. *Lett*. **2002**, *80*, 4606–4608.

[62] Jeong, C. K.; Kim, I.; Park, K.-I.; Oh, M. H.; Paik, H.; Hwang, G.-T.; No, K.; Nam, Y. S.; Lee, K. J. Virus-directed design of a flexible $BaTiO_3$ nanogenerator. *ACS Nano* **2013**, *7*, 11016–11025.

[63] An, Y.-K.; Sohn, H. Visualization of non-propagating lamb wave modes for fatigue crack evaluation. *J*. *Appl*. *Phys*. **2015**, *117*, 114904.

[64] Kim, J.; Kim, K.; Sohn, H. *In situ* measurement of structural mass, stiffness, and damping using a reaction force actuator and a laser doppler vibrometer. *Smart Mater*. *Struct*. **2013**, *22*, 085004.

[65] Zhou, Z.; Tang, H. X.; Sodano, H. A. Scalable synthesis of morphotropic phase boundary lead zirconium titanate nanowires for energy harvesting. *Adv*. *Mater*. **2014**, *26*, 7547–7554.